



Unconventional magnonic surface and interface states in layered ferromagnets

Khalil Zakeri ¹✉, Huajun Qin^{1,2} & Arthur Ernst ^{3,4}

Electronic surface, interface and edge states are well-known concepts in low-dimensional solids and have already been utilised for practical applications. It is expected that magnons—the bosonic quasiparticles representing the magnetic excitations—shall also exhibit such exotic states. However, how these states are formed in layered magnetic structures is hitherto unknown. Here we bring the topic of magnonic surface and interface states in layered ferromagnets into discussion. We provide experimental examples of synthetic layered structures, supporting our discussions and show that these states can be tailored in artificially fabricated structures. We demonstrate that the magnonic surface or interface states may show peculiar features, including “standing” or “ultrafast” states. We argue that these states can drastically change their electronic and magnonic transport properties. In this way one can design layered ferromagnets which act as magnon conductor, semiconductor and insulator of specific states.

¹Heisenberg Spin-dynamics Group, Physikalisches Institut, Karlsruhe Institute of Technology, Karlsruhe, Germany. ²NanoSpin, Department of Applied Physics, Aalto University School of Science, Aalto, Finland. ³Institute for Theoretical Physics, Johannes Kepler University, Linz, Austria. ⁴Max-Planck-Institut für Mikrostrukturphysik, Halle, Germany. ✉email: khalil.zakeri@partner.kit.edu

The concept of the electronic band structure is one of the most important concepts in condensed-matter physics. It is essentially used to describe the electron dynamics in solids and thereby understand their macroscopic properties^{1–3}. The concept was first developed by Bloch in the early days of quantum theory of solids⁴. Soon after, it was realized that the presence of surface and interface can lead to additional electronic bands and hence the concepts of surface and interface states were introduced^{5–7}. Generally, based on Bloch's theorem, the eigenstates of the single-electron Schrödinger's equation with a perfectly periodic potential are the so-called Bloch states. The termination of a crystal at the surface (or interface) causes deviations from perfect periodicity. Consequently, if the periodic boundary conditions are abandoned in the direction normal to the surface (or interface), the behavior of electrons will deviate from their behavior in the bulk and leads to the formation of new electronic states, that is, surface (or interface) states. The most prominent examples of surface states are those observed at the surface of some noble metals. Examples of this kind are the Shockley and Tamm states^{5–7}. The interface states, on the other hand, have mainly been discussed in semiconductor heterostructures, where two different materials are brought together⁸. They obey somewhat the same physics as those of the surface states. The main difference, however, is that the periodic potential is not abruptly changed into the vacuum level, but it is changed into a different potential level, which can then be periodic. Hence, more scenarios are expected in the latter case⁸.

Note that the Shockley and Tamm states are not conceptually different. In fact, there is no real physical distinction between these two. The only difference is that the mathematical approach in describing the surface states is different. The condition under which the surface states can exist and the differences between Tamm and Shockley states are discussed in ref. ⁹. The mechanism of Tamm is suitable to describe wide bandgap semiconductors. Shockley states are normally states that arise due to the abrupt change in the electron potential associated solely with the crystal termination. This approach is suitable to describe metals like Cu, Ag, and Au, and narrow bandgap semiconductors. Generally, the band-center operator and the Berry phase may be used to investigate the gap between the bands of specific symmetry, supporting the existence of the surface states¹⁰.

Low-dimensional solids with confined geometries, for example, thin films with finite thicknesses, exhibit also surface or interface states. In such structures, the effects associated with quantum confinement (quantum size effects or quantum well states) are also present^{1,7}.

The concept of surface states became more interesting after the discovery of the topologically protected surface states in topological materials, for example, topological insulators and Dirac and Weyl semimetals^{11–15}. The most prominent property of these surface states is that they are topologically protected and are, therefore, robust against external perturbations. This fact makes these materials promising candidates for utilizing surface states in practical devices.

Surface and interface states are not only limited to the fermionic Bloch states. The bosonic quasiparticles in a truncated solid and in heterostructures can exhibit surface and interface states¹⁶. Although such states have been the topic of several theoretical considerations, they have rarely been addressed in the experiments. The concept of bosonic surface, interface, and edge states has recently become very attractive in the context of topologically protected bosonic states^{17–19}. It is theoretically predicted and experimentally confirmed that under some circumstances such topologically protected states are present in layered materials^{18–25}. Special attention has been paid to magnons, as the bosonic quasiparticles of spin excitations in a

magnetic solid. This is due to the fact that these excitations can, in principle, be utilized in the new generation of devices, for example, in magnonics. However, how the magnonic band structure is formed in a system composed of alternating ferromagnetic layers, how such a magnonic band structure develops with increasing the number of atomic layers, how the surface and interface states enter the picture, and how can be tailored is hitherto experimentally unexplored.

It is important to note that in the case of layered ferromagnets with a finite number of atomic layers, the definition of surface and interface states is not exactly the same as the one conventionally used for semi-infinite crystals. In the present case, the effects associated with the quantum confinement in the direction perpendicular to the layers become of great importance. Moreover, one needs to find a way to assign the observed bands to the surface and interface layers.

Here, by investigating model systems of atomically engineered epitaxial layered ferromagnets, we bring the topic of magnonic surface and interface states, formed in structures composed of a finite number of atomic layers, into discussion. We provide the experimental results, obtained using spin-polarized high-resolution electron energy-loss spectroscopy (SPEELS), and combine them with accurate theoretical calculations. We first start with the concept of the magnonic band structure in layered ferromagnets and discuss the physics of the band formation in such structures. We discuss the origin of the bands with respect to their real-space localization and provide new insights into the origin of the magnonic bands. We use the concept of the real-space localization of the magnons and their layered-resolved density of states (DOS) to distinguish between, surface, interface, and interior magnon states. We then outline the circumstances under which the surface and interface states are formed. We further provide experimental examples for each case, supporting our discussions. We experimentally demonstrate how these states may be tailored in atomically designed synthetic structures. Moreover, we demonstrate that under some conditions, the surface or interface states show peculiar features, including “standing bosonic Bloch states” or “states with the ultrahigh group velocity.” We discuss how these states may change the properties of the material and how they influence the magnon dynamics as well as the electron transport in designed heterostructures.

Results

The concept of electronic band structure originates from the Bloch states in a periodic potential. The Bloch states are the eigenstates of a Schrödinger-like equation, which is invariant under translation symmetry. In the case of bosonic excitations such as magnons, the relevant Hamiltonian is the one known as the Heisenberg Hamiltonian. The solutions of this Hamiltonian are also Bloch states. One can show that such states for a single-element ferromagnetic solid with only one atom in the unit-cell degenerate in energy, forming only a single magnonic band. In fact, the number of magnonic bands is equal to the number of unit cells. Due to the perfect periodicity, all bands degenerate in energy, forming a single magnonic band. In the case of a semi-infinite truncated magnetic solid, one has to introduce the surface effects. This can easily be done by assuming that the magnon wavevector in the direction perpendicular to the surface is a complex number. This fact leads to two sets of solutions, that is, the surface and volume modes, as the consequence of the imaginary and real part of the perpendicular magnon wavevector^{26–31}.

In the case of a system composed of a finite number of atomic slabs, the situation is somewhat different. The degeneracy of the

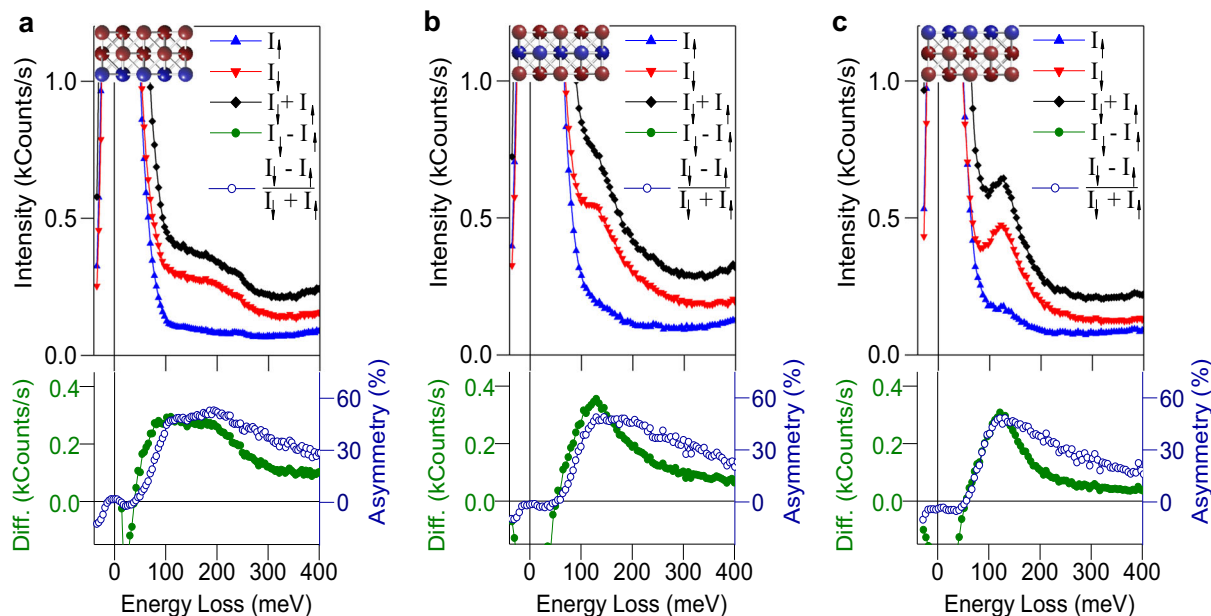


Fig. 1 Spin-polarized high-resolution electron energy-loss spectra recorded on different layered structures. The spectra are recorded at a wavevector of $q_{\parallel} = 1 \text{ \AA}^{-1}$ along the $\bar{\Gamma}-\bar{X}$ of **a** Co/Co/Fe, **b** Co/Fe/Co, and **c** Fe/Co/Co, all grown on Ir(001). I_{\parallel} and I_{\uparrow} represent the intensity spectra when the spin polarization of the incoming electron beam was parallel and antiparallel to the minority spins of the sample. The sum ($I_{\parallel} + I_{\uparrow}$), difference ($I_{\parallel} - I_{\uparrow}$), and asymmetry ($\frac{I_{\parallel} - I_{\uparrow}}{I_{\parallel} + I_{\uparrow}}$) spectra are also shown. In all three examples, several magnon modes are visible in the spectra. The geometrical structures of the investigated layered structures are depicted as the insets (blue and red spheres represent Fe and Co atoms, respectively).

magnon bands is lifted, due to the broken translation symmetry in the direction perpendicular to the layers, and hence several magnon bands are expected, including surface and interface states^{26–28}. Note that although there are differences between the surface states of a finite system and the conventional surface states of a semi-infinite crystal, they share several common features (see the discussion below). In order to illustrate these effects, we consider synthetic ferromagnetic layered structures, ordered in face-centered tetragonal structure, with one complete unit cell. To fulfill this condition, one requires three atomic layers. Another important consideration is that, since these layers are epitaxially grown on a substrate one deals with three distinct atomic layers, which are inherently different, that is, surface, interior, and interface layer. In order to see how the magnonic band structure is formed in such structures, we measure and compare three systems: (i) Co/Co/Fe, (ii) Co/Fe/Co, and (iii) Fe/Co/Co. All three systems are grown on Ir(001). The main idea is to create different surface and interfaces and thereby see how the magnonic bands are formed and what is the contribution of different parts of the unit cell to the band structure. For details on the sample preparation and characterization, see “Methods.”

In Fig. 1, the SPEELS spectra recorded at the wavevector of $q_{\parallel} = 1 \text{ \AA}^{-1}$ along the $\bar{\Gamma}-\bar{X}$ direction of the surface Brillouin zone (SBZ) are presented. The spectra recorded with different spin polarization vectors of the incoming electron beam (I_{\parallel} and I_{\uparrow}) and the sum spectra ($I_{\parallel} + I_{\uparrow}$) are shown in the upper panel. The difference ($I_{\parallel} - I_{\uparrow}$) and the asymmetry ($\frac{I_{\parallel} - I_{\uparrow}}{I_{\parallel} + I_{\uparrow}}$) spectra are shown in the lower panel. In all three systems, one clearly observes the signature of different magnon modes in the spectra. While in the case of Co/Co/Fe and Co/Fe/Co the peaks associated with different magnon modes are well separated, in the case of Fe/Co/Co they are close in energy and mainly one single peak is dominating the spectra. In order to probe the magnonic band structure, the spectra were recorded at different values of q_{\parallel} and along the main symmetry directions of SBZ.

Bloch spectral function of magnonic band structure. The magnonic band structure probed in Co/Co/Fe, Co/Fe/Co, and Fe/Co/Co systems is presented in Fig. 2a–c, respectively. The results are compared to those of three atomic layers of Co grown on the same substrate, shown in Fig. 2d. The reason for choosing these synthetic multilayers is that Co/Co/Fe and Co/Co/Co systems share the same surface but different interfaces. In contrast, Co/Fe/Co and Co/Co/Co systems share the same surface and interface, but they differ in the interior layer. The Fe/Co/Co, Co/Fe/Co, and Co/Co/Co systems share the same interface layer and differ in the surface and interior layers. A comparison among all these systems would allow to experimentally separate the contributions of different atomic layers to the magnonic band structure.

The magnonic band structure in Fig. 2 is constructed by plotting the Bloch spectral function (BSF) of magnons, calculated for each system. The experimental data are shown by symbols. As it is apparent from Fig. 2, all systems exhibit three magnon bands associated with different quantum numbers $n = 0, 1, \text{ and } 2$. Here, n represents the emergent quantum confinement in the magnonic Bloch states in the direction perpendicular to the layers (under the assumption of unpinned spins at the surface and interface the perpendicular component of the wavevector q_{\perp} is given by $q_{\perp} = q_z = n\pi/md$, where $m = 3$ is the number of atomic layers and d is the thickness of one atomic layer in the units of angstrom, see the discussion below).

Note that the description of the magnonic band structure provided above is general. As no additional assumption is considered, the resulting magnonic band structure includes all the possible states including surface, interface, and interior states. It will be shown that the assignment of the magnons to the surface, interior, and interface layer can be done based on the layer-resolved BSF or the magnonic DOS (a similar approach is used for the electronic states, in order to assign the bands to different parts of the structures). In the limit of $m \gg 1$ one may assume that q_{\perp} is a complex quantity. Under such an assumption, the surface

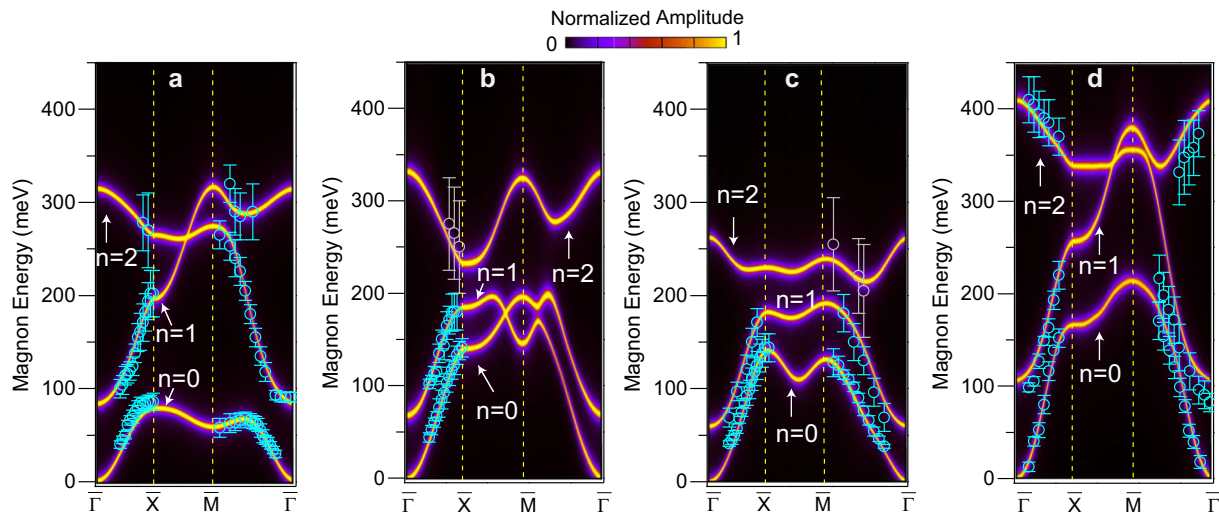


Fig. 2 The magnonic band structure of different layered structures. The results are presented for the **a** Co/Co/Fe, **b** Co/Fe/Co, **c** Fe/Co/Co, and **d** Co/Co/Co systems. The calculated band structure is represented as the Bloch spectral function of magnons in all three layers. The experimental data are shown by symbols. The data shown by the cyan color are based on the analysis of the difference spectra. The data represented by the light-gray color are based on the analysis of the asymmetry spectra. While in the case of Co/Co/Fe the $n = 0$ and $n = 1$ magnon bands are very different in their shape, in the case of Co/Fe/Co they exhibit a rather similar shape. The error bars represent both the statistical and systematic uncertainties (see “Methods” section). In all panels, $\bar{\Gamma}$, \bar{X} , and \bar{M} represent the high symmetry points of the surface Brillouin zone.

modes are determined by the imaginary part of q_{\perp} and the bulk modes are the consequence of the real part of q_{\perp} . One can show that the same can be concluded assuming a large but a finite m and analyzing the magnonic BSF or DOS.

Comparing the results of the Co/Co/Fe and Co/Fe/Co to those of the Co/Co/Co system, one notices that the magnonic band structure is very much different, even though all systems show nearly the same geometrical structure. A noticeable difference was observed when comparing the magnonic band structure of Co/Co/Fe with the one of Co/Fe/Co. In order to shed light on the origin of this effect, one way would be to calculate the spectral function of the magnonic Bloch states and see how the magnonic bands are formed leading to the observed magnonic band structure. To this end, we calculate and compare the BSF of the magnonic states in the momentum space, in a way similar to that of the Bloch electronic states in solids. BSF can be projected onto different parts of the unit cell in order to separate the contribution of different atoms to the magnonic bands. Moreover, the magnon density of states (DOS) can be calculated by integrating the BSF over the momentum space. In the same way, the partial magnon DOS of each atomic layer can be calculated by integrating the projected BSF on that particular layer.

The magnonic band structure presented in Fig. 2a reveals that in the case of the Co/Co/Fe system, a magnonic bandgap is opened along the $\bar{\Gamma}$ - \bar{M} between the $n = 0$ and $n = 1$ magnon modes. Likewise, the $n = 1$ and $n = 2$ are also separated by a bandgap of ~ 20 meV along the $\bar{\Gamma}$ - \bar{M} direction and by a bandgap of ~ 70 meV along the $\bar{\Gamma}$ - \bar{X} direction. In the case of the Co/Fe/Co and Co/Co/Co systems, the bandgap is opened only between the $n = 1$ and $n = 2$ bands. The magnitude of the bandgap in the case of the Co/Fe/Co system is ~ 80 meV along the $\bar{\Gamma}$ - \bar{M} and ~ 50 meV along the $\bar{\Gamma}$ - \bar{X} direction. This bandgap for the case of Co/Co/Co is ~ 85 meV (a detailed discussion on the magnonic band gaps maybe found in ref. 32).

BSF of the Co/Co/Fe system described in Fig. 2a is presented in Fig. 3a–d. We show the spectral function projected into all three atomic layers and compare the results to those projected into individual atomic layers. The total BSF of the Co/Co/Fe system is shown in Fig. 3a. The BSF projected into the interface, middle,

and surface layer is presented in Fig. 3b–d, respectively. In this system, the main contribution to the magnon band with $n = 0$ originates from the Fe atoms located next to the Ir substrate. This is due to the fact that the BSF of this mode exhibits the largest spectral weight when it is projected into the interface Fe layer. Looking at the density of magnon states, presented in Fig. 3e, one ends up with the same conclusion. The magnon DOS projected into different layers indicates that the low-energy part of the spectrum is mainly localized in the interface layer, that is, in the Fe layer. Likewise, the middle part of the spectrum is governed by the magnons localized in the topmost Co layer. Finally, the high-energy part of the spectrum describes the magnons localized in the middle layer (see Fig. 3c). The Bloch states of the $n = 1$ magnon band are mainly localized in the topmost Co layer, since this mode has the largest spectral weight when it is projected into this layer. We note that the localization of the magnon bands can analogously be explained considering magnons as classical waves (the same is correct for other quasiparticles). However, the quantum mechanical description of magnons provides an unambiguous way of determining their characteristics such as their BSF and DOS. Moreover, such a description is more realistic for high-energy, high-wavevector magnons and provides a rather complete picture of the experimental results. The very strong spatial localization of the $n = 0$ and $n = 1$ magnon modes has consequences on the real-space propagation of the magnon states. We come back to this point later in the “Discussion” section, where we describe the real-space propagation of magnons.

In the case of Co/Fe/Co/Ir(001), however, the pattern of the spectral function is inherently different. These patterns are presented in Fig. 3f–i. BSF projected into all three layers is presented in Fig. 3f. The projected BSF into the interface, middle, and surface layers is shown in Fig. 3g–i, respectively. Comparing the spectral functions presented in Fig. 3g, h indicates that the contributions of the first two layers to the first two magnon modes (the mode with $n = 0$ and $n = 1$) are nearly equal. This fact is also reflected in the partial density of magnon states plotted in Fig. 3j, revealing that the lower part of the spectrum is governed by the magnons localized in these two layers. This observation is very interesting even though the first two layers are

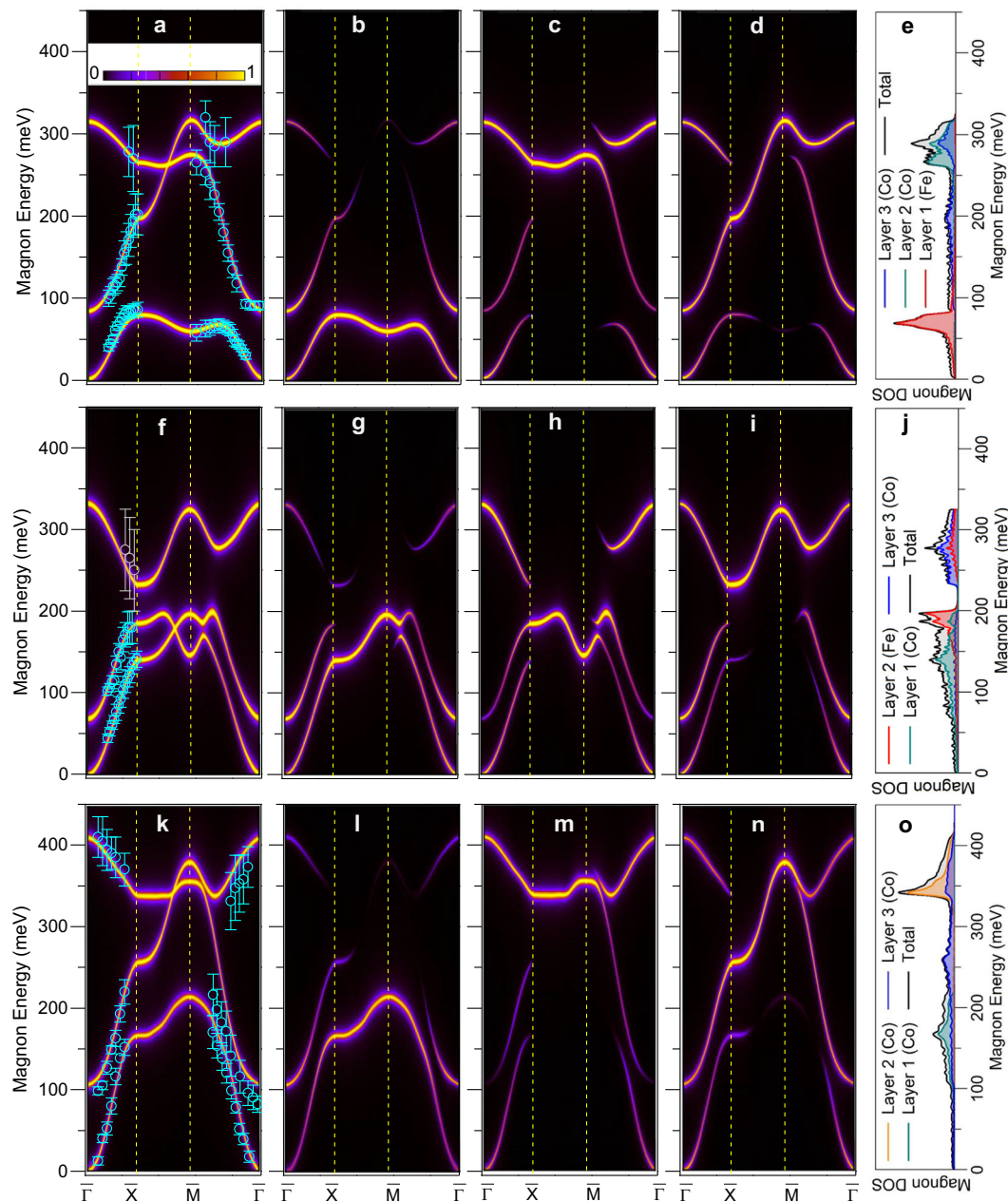


Fig. 3 The magnon Bloch spectral function and density of magnonic states (DOS) of different layered structures. Co/Co/Fe (a–e), Co/Fe/Co (f–j), and Co/Co/Co (k–o). The total Bloch spectral function of Co/Co/Fe is presented in panel (a) and the projected Bloch spectral function into the interface, middle, and surface layer is shown in panels (b, c, and d), respectively. The total and layer-resolved magnon density of states are shown in panel (e). The total Bloch spectral function of Co/Fe/Co is presented in panel (f) and the projected Bloch spectral function into the interface, middle, and surface layer is shown in panels (g, h, and i), respectively. The total and layer-resolved magnon density of states are shown in panel (j). The total Bloch spectral function of Co/Co/Co is presented in panel (k) and the projected Bloch spectral function into the interface, middle, and surface layer is shown in panels (l, m, and n), respectively. The total and layer-resolved magnon density of states are shown in panel (o). The experimental data are shown by the symbols. The data shown by the cyan color are based on the analysis of the difference spectra. The data represented by the light-gray color are based on the analysis of the asymmetry spectra. The error bars represent both the statistical and systematic uncertainties (see “Methods” section). In all panels, $\bar{\Gamma}$, \bar{X} , and \bar{M} represent the high symmetry points of the surface Brillouin zone.

made of different materials. The results are also different from those of the Co/Co/Co system, presented in Fig. 3k–o. Here again, the $n = 0$ magnon band is mainly localized in the interface Co layer. The middle and topmost layer host mainly the $n = 2$ and $n = 1$ magnon bands, respectively.

The differences in the shape as well as in the spatial localization of different magnonic bands, observed for the different synthetic ferromagnetic layered structures, are a consequence of different

patterns of the magnetic exchange parameters in these systems³³. The $n = 0$ magnon mode of the Co/Co/Fe/Ir(001) system is almost a perfect interface mode due to the fact that the magnetic exchange parameters in the Fe layer next to the Ir substrate are very weak^{34–36}. This fact leads to a soft magnon mode, which lies below other magnon bands. This mode represents a magnon mode, which has the largest spectral weight when it is projected into the interface layer. Consequently, the magnon mode with

$n = 1$ is almost purely a surface mode, which is characterized by its large spectral weight when it is projected into the surface Co layer. Although the mode with $n = 2$, lying in the high-energy part of the spectrum, is mainly an interior mode, which is localized in the middle Co layer, it is also partially localized in the surface Co layer. While the energy of the $n = 1$ magnon mode increases with the wavevector, the one of the $n = 0$ mode shows an unexpected behavior, that is, undergoes an extremum before the zone boundary. This is the signature of a complex pattern of intralayer exchange parameters. Generally, if a ferromagnetic material is grown on a substrate in the form of a monolayer (ML). The values and the character of the exchange coupling constants can be very different from those of the bulk^{37,38}. For example, the nearest-neighbor exchange constant can be positive (ferromagnetic character) and the next-nearest-neighbor exchange constant can be negative (antiferromagnetic character). The reason is twofold: (i) the geometrical structure as a result of the film epitaxy, and (ii) the hybridizations of the electronic structures of the film with those of the substrate. The situation is more complex if one increases the number of atomic layers. In this case, the pattern of the exchange parameters will be very complex through the whole structure, meaning that some exchange constants can be positive and some negative^{34,35}.

Similarly, one may analyze the BSF of the Fe/Co/Co system and its projection into different layers. Such data are provided in the Supplementary Fig. 1. The analysis reveals that the $n = 0$ and $n = 1$ magnon modes of this system are mainly localized in the surface (Fe) and interface (Co) layer, respectively. However, the degree of localization is not as strong as in the Co/Co/Fe system. The $n = 2$ magnon band is strongly localized in the middle Co layer, similar to the other systems, discussed above (for a discussion see the Supplementary Note 1).

As a side remark, further analyses of the investigated magnon bands in all the measured systems revealed that they do not exhibit detectable topological properties. This is due to the small Dzyaloshinskii–Moriya interaction (DMI), compared to the Heisenberg exchange and also the symmetry of the systems.

Magnetic anisotropy is an important concept in ultrathin magnetic films and multilayers. To see the consequence of this term on the magnonic band structure, one just needs to know how it enters the spin Hamiltonian. The anisotropy term has the form of $\mathcal{H}_{\text{An}} = -\frac{1}{2} \sum_i K(\mathbf{S}_i \cdot \hat{\mathbf{e}})^2$. Here K denotes the effective magnetic anisotropy constant, \mathbf{S}_i represent the spins on site i and $\hat{\mathbf{e}}$ represents the direction of the easy axis. The consequence of this term is that it opens up a very small gap for the $q_{\parallel} = 0$ magnons, that is, at the $\bar{\Gamma}$ point^{37,39}. The gap is directly proportional to K and is on the order of μeV , which is several orders of magnitude smaller than the energies considered here.

Constant energy slices. In order to investigate the momentum and real-space localization of different magnon bands, we analyze the two-dimensional momentum space distribution of magnons in different layers. To this end, we calculate the so-called constant energy slices of BSF and their projections into different layers. Figure 4 shows the constant energy slices of the magnonic bands of the three systems discussed above. In this representation, the magnon BSF is shown in the q_x - q_y momentum space (here the subscripts x and y denote the main in-plane axes). Since for each energy this distribution is different, we show the momentum contours for several energy cuts. The positions of the magnon peaks as observed in the experimental spectra are indicated by solid circles.

For simplicity let us start the discussion with the Co/Co/Co system. The results of this system are presented in Fig. 4a–d. While the total BSF of all layers is shown in Fig. 4a, the projected

BSF into the interface, middle, and surface layers is shown in Fig. 4b–d, respectively. In this case for energies < 100 meV one observes a ring-like pattern of BSF in the two-dimensional momentum space. The diameter of the ring increases with energy. At ~ 100 meV another ring associated with the $n = 1$ magnon mode appears and the pattern evolves into a pattern with two centered rings. The diameter of the two rings increases with energy. The ring corresponding to $n = 0$ disappears at the edges of SBZ at an energy of ~ 220 meV. The one corresponding to the $n = 1$ magnon mode disappears at an energy of ~ 350 meV. At this energy, a new mode appears from the edges of SBZ, that is, the $n = 2$ magnon mode. Since this mode exhibits a negative group velocity, it first appears as a ring with a large diameter. The diameter of the ring decreases with energy. The projected momentum space distribution of magnon modes, shown in Fig. 4b–d, indicates that the low-energy part of the magnon spectrum (energies < 200 meV) has the largest spectral weight when it is projected into the interface Co layer. This part of the spectrum corresponds to the $n = 0$ and partially $n = 1$ magnon mode. In contrast, the high-energy part of the spectrum (energies > 350 meV) has the largest spectral weight, when the pattern is projected into the middle Co layer. Finally, the middle part of the magnon spectrum has its largest spectral weight when it is projected into the surface Co layer. Interestingly, the spectral weight of the other parts of the magnon spectrum on this layer is considerable. This is perhaps the most important feature of the system, which leads to the efficient excitation of all three magnon modes using low-energy electrons. Summarizing the above discussion, the Co/Co/Co system represents a case in which the interface Co layer has the largest contribution to the low-energy part of the spectrum. The surface layer has the largest contribution to the middle part of the spectrum and also a finite contribution to all the other magnonic bands. The high-energy part of the spectrum is mainly governed by the middle Co layer. A similar conclusion may be drawn by looking at the magnonic DOS presented in Fig. 3e.

The constant energy slices of the magnonic bands for the case of Co/Co/Fe is shown in Fig. 4e–h. Again the total BSF of all layers is shown in Fig. 4e and the projected BSF into the interface, middle, and surface layer is shown in Fig. 4f–h, respectively. As it is apparent from Fig. 4e, the ring-like pattern of the $n = 0$ magnon modes evolves into a double ring structure at an energy of ~ 60 meV. This is an unusual behavior, since at this energy only the $n = 0$ magnon band should exist. The second ring appears from the edges of the SBZ and moves towards the zone center, while going to higher energies. This peculiar behavior is a result of the complex real-space pattern of magnetic exchange parameters in the interface Fe layer. The competition of different exchange parameters leads to an unusual magnon band, which undergoes an extremum in the midway of $\bar{\Gamma}$ - \bar{M} . This has very interesting consequences on the real-space localization of magnons (see the “Discussion” section). The spectral function projected into different layers is presented in Fig. 4f–h. Looking at the projected magnon BSF on the interface Fe layer (Fig. 4f), one realizes that the low-energy part of the magnon spectrum (energies < 100 meV) and in particular the $n = 0$ magnon mode is entirely localized in the interface Fe layer. The degree of localization is much higher than the case of Co/Co/Co system. The intermediate- and high-energy part of the magnon spectrum is localized in the top two Co layers. The fast increase of the size of the square-like pattern of the $n = 1$ magnon mode with energy indicates a rather high group velocity of this magnon mode.

The constant energy slices of the magnonic band structure for the case of Co/Fe/Co is presented in Fig. 4i–l. The total BSF of all layers is shown in Fig. 4i and the projected BSF into the interface,

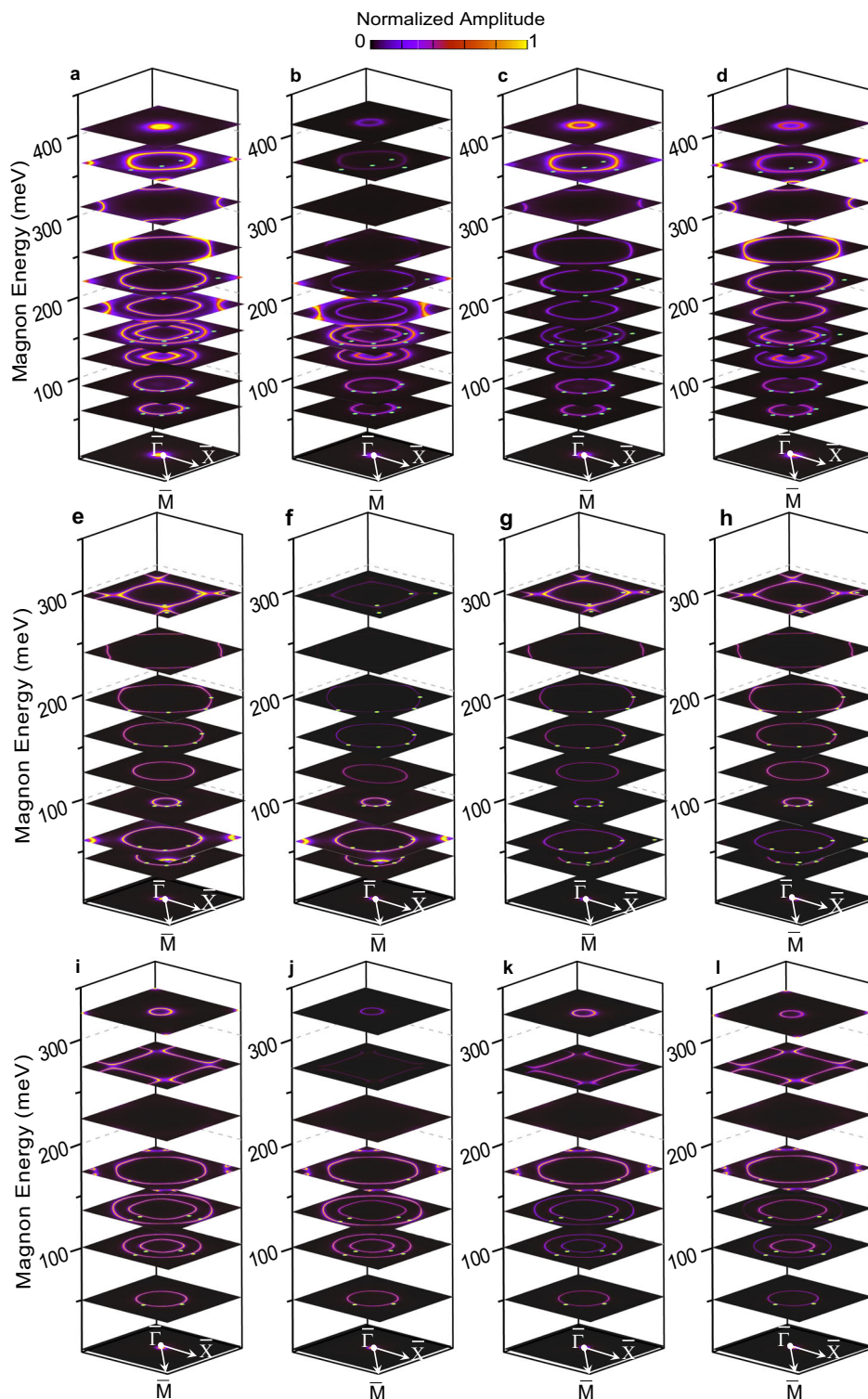


Fig. 4 Two-dimensional momentum maps at fixed energies. Panels **a–d** represent the Co/Co/Co system. **a** The spectral function projected into all three layers, **b** into the interface layer, **c** into the middle layer, and **d** into the surface layer. Panels **e–h** represent the Co/Co/Fe system. The projected Bloch spectral function into all three layers, the interface layer, the middle layer, and the surface layer, is shown in panels (**e, f, g, h**), respectively. The results of the Co/Fe/Co system are shown in panels (**i–l**), where the projected Bloch spectral function into all three layers, the interface layer, the middle layer, and the surface layer is shown in panels (**i, j, k, l**), respectively. The places where the magnon peaks are observed in the experimental spectra are shown by solid circles. In all panels, $\bar{\Gamma}$, \bar{X} , and \bar{M} represent the high symmetry points of the surface Brillouin zone.

middle, and surface layer is shown in Fig. 4j–l, respectively. In this case, the low-energy part of the magnon spectrum is distributed over all three layers. This part includes the $n=0$ and $n=1$ magnon modes of the system. The configuration of the exchange

constants is such that the resulting magnon bands representing these two modes are similar and behave like two parallel parabola in the energy–momentum space. Interestingly, the intermediate part of the magnon spectrum is almost equally localized in all

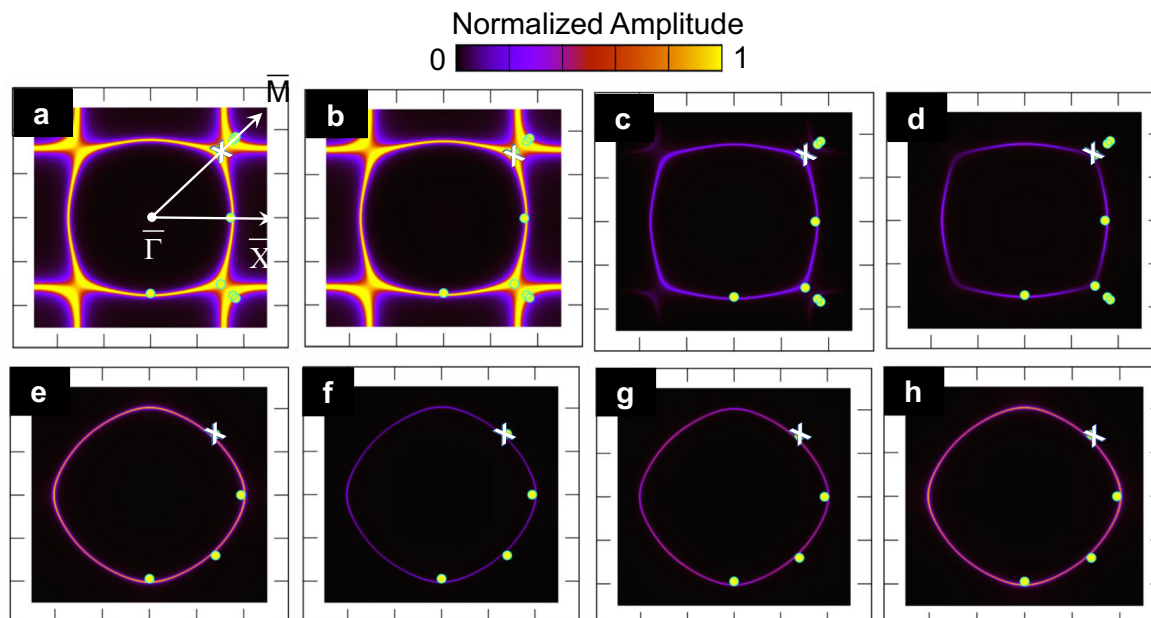


Fig. 5 Two-dimensional momentum space distribution of magnons in the Co/Co/Fe system. The energy cuts are chosen so as to highlight the in-plane wavevector of 1 \AA^{-1} along the high symmetry $\bar{\Gamma}$ - \bar{M} ($\bar{\Gamma}$ and \bar{M} represent the high symmetry points of the surface Brillouin zone). Panels **a-d** show the results for the magnon energy of 66 meV (magnons with $n=0$) and **e-h** are the results for the magnon energy of 180 meV (magnons with $n=1$). The total Bloch spectral function is shown in panels (**a**, **e**). The Bloch spectral function projected into the interface (**b**, **f**), middle (**c**, **g**), and surface layer (**d**, **h**) is also shown.

three layers. The high-energy part of the magnon spectrum, which mainly includes the $n=2$ magnon mode, is mostly localized in the top two layers (mainly the surface Co layer).

We would like to emphasize that the unconventional properties of surface/interface magnons described above are due to the complex pattern of the magnetic exchange interaction in these systems. Considering only the periodicity and symmetry breaking in the system would not explain the observed effects. We show experimentally that the complex pattern of the exchange interaction in these layered structures can be used to tailor the magnonic band structure of these systems as well as the spatial localization of different magnon bands.

Discussion

As pointed out earlier, the magnonic band structure of different systems exhibits unusual and unique features. Taking the Co/Co/Fe as an example, the $n=0$ magnon mode undergoes an extremum at the midway of $\bar{\Gamma}$ - \bar{M} direction. The complex pattern of the exchange interaction in this system leads to such interesting effects in the magnonic band structure. Note that this point is not a high symmetry point. In contrast, the $n=1$ magnon mode shows an expected monotonous behavior. These two effects have direct consequences on the magnon wave packets, which describe the two magnon modes. In order to illustrate this, we construct the magnon wave packets representing these two modes. For that, we focus on the wavevector of $q_{\parallel} = 1 \text{ \AA}^{-1}$ along the $\bar{\Gamma}$ - \bar{M} direction (this means $q_x = q_y = 0.71 \text{ \AA}^{-1}$) and discuss how these wave packets evolve in real time and real space.

In Fig. 5a-d the two-dimensional momentum map of the spectral function of the magnon mode with $n=0$ and the energy of 66 meV are presented. The total spectral function is shown in Fig. 5a and the projected spectral function into the interface, middle, and surface layer is shown in panels b-d, respectively. We aim to construct the magnon wave packet in the point marked with the cross, that is, $(q_x, q_y) = (0.71, 0.71)$ (the values are given in the units of \AA^{-1}). Since at this point the dispersion relation of

the $n=0$ magnon mode shows a broad maximum, the distribution of the mode in the two-dimensional momentum space is rather broad. This is in contrast to the $n=1$ magnon mode, which shows a narrow distribution (see Fig. 5e for the two-dimensional momentum space distribution of the $n=1$ magnon mode at the wavevector of $(q_x, q_y) = (0.71, 0.71)$ and energy of 180 meV). The projected spectral function of this mode into the interface, middle, and surface layer is shown in Fig. 5f-h, respectively. The fact that the magnons with $n=0$ represent the interface states and those with $n=1$ represent the surface states can easily be concluded by comparing the projected BSF of these modes into the surface and interface layers (compare Fig. 5b-d and f-h).

Since we have now all the required information regarding the real-space localization of magnons and also their group and phase velocities, we can provide the real-space representation of magnon wave packets representing these two modes. To this end, we have constructed the magnon wave packets from the experimental data in the same way as described earlier⁴⁰⁻⁴². Generally, the magnon wave packet is a result of the Fourier transformation of the experimental magnon signal measured in the momentum-energy space.

Looking at the experimentally measured intensity profile in momentum-energy space, one realizes that the measured magnon signal shows a broadening in momentum and a broadening in energy. In order to construct the wave packet from the experimental data, both the distribution in momentum and in energy are important and have to be taken into account. This has been considered in our analysis via two steps. In the first step, we considered the momentum space broadening of the magnon spectra. In the second step, we considered the energy space broadening of the spectra by entering the experimental lifetime of the magnon wave packet τ_n (the superscript n refers to the mode number) into the analysis. The lifetime is inversely proportional to the intrinsic broadening of the magnon mode in energy Γ_n by $\tau_n = 2\hbar/\Gamma_n$. Our analysis reveals that in the case of Co/Co/Fe, the lifetime is $\tau_0 = 33 \text{ fs}$ and $\tau_1 = 15 \text{ fs}$ for the $n=0$ and $n=1$

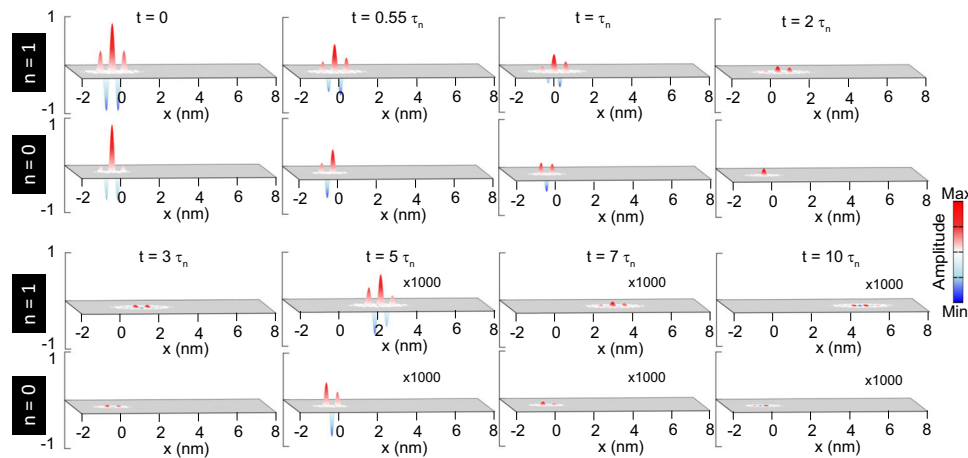


Fig. 6 Real-space evolution of surface and interface magnons in the Co/Co/Fe structure. The evolution of the magnon wave packets in the Co/Co/Fe structure at the point $(q_x, q_y) = (0.71, 0.71)$, indicated in Fig. 5. Here, q_x and q_y represent the x and y components of the wavevector. τ_n denotes the lifetime of the n th magnon mode and is obtained from the experimental data ($\tau_n = 2\hbar/\Gamma_n$, where Γ_n represent the intrinsic broadening of the magnon modes, $\tau_0 = 33$ fs and $\tau_1 = 15$ fs). The amplitude of the wave packets after $t = 5\tau_n$ is multiplied by 1000 for clarity. The $n = 0$ mode does not propagate, indicating its standing-wave characteristics, while the $n = 1$ mode propagates over 5 nm within $t = 150$ fs.

magnon modes, respectively. In layered structures discussed here, we further considered the real-space localization of the magnons while constructing the wave packets. This is done by taking into account the layer-resolved spectral function. The resulted wave packets and their real-time dynamics are illustrated in Fig. 6.

The magnitude of the group velocity of the magnon wave packet at the point q_0 is given by $v_g = \frac{\partial \omega}{\partial q} \Big|_{q_0}$. For the wave packet with $n = 0$ and the point indicated by the cross in Fig. 5, the group velocity is zero. The wave packet represents a “standing wave” that is mainly localized in the Fe layer. It is extremely important to notice that the observed zero group velocity, which leads to the formation of standing magnon states, does not take place at the high symmetry points. Surprisingly, it occurs somewhere in the midway of the high symmetry $\bar{\Gamma}$ – M direction of SBZ. The phase velocity at the point $(q_0, \hbar\omega_0)$ is given by $v_p = \frac{\omega_0}{q_0}$. Our analysis indicates that this magnon wave packet possesses also a rather low phase velocity of about $v_p = 10$ km s⁻¹, since the energy of this mode is rather low. In contrast, the magnon mode with $n = 1$, which represents a surface mode travels rather fast. It travels with a group velocity as large as $v_g = 34.1$ km s⁻¹ and possesses a phase velocity as high as $v_p = 27.4$ km s⁻¹. This wave packet is entirely localized at the Co layers and mainly in the surface Co layer (see Fig. 5g, h). Hence, it represents a “true” surface mode.

Interestingly, in a similar manner, one can show that the group velocity of the $n = 2$ magnon mode of this system is also zero and the wave packet associated with this magnon mode behaves also as a “standing wave.” This is due to the fact that this magnon band undergoes a minimum at this point (see, for example, Fig. 2a). Our results indicate that the Co/Co/Fe/Ir(001) system may be considered as an “interface and bulk magnon insulator.” Such a system exhibits no magnon conductivity at the interface and in the interior of the film but a high magnon conductivity at the surface. It, therefore, may represent “ultrafast magnonic surface states.” This observation is important for the processes that involve magnons and their dynamics. Examples are magnetotransport properties of epitaxial heterostructures (known as tunnel magnetoresistance and giant magnetoresistance structures)^{43–54}. Furthermore, the results are also important in the context of static and dynamic properties of magnetic heterostructures, as these properties are tightly connected to the properties of magnons in these structures. Another important

consequence of the observed effect is that it can largely influence the phenomenon of magnetization reversal using spin-polarized currents, spin Hall, or spin torque effects, as these effects are associated with the coupling of the electrons’ spins to the interface magnetic moments and their dynamics. Taking the phenomenon of current-induced magnetization reversal as an example, in order to excite and finally reverse the magnetization of the magnetic layer, an efficient coupling of the spin of the transport electrons to the magnetic moments of the ferromagnetic layer is essential^{43–54}. Such a coupling can efficiently be enhanced by involving the interface magnons. If such magnons have standing character, an enhanced coupling is expected. We note that in most of these devices mainly the dipolar magnons with very small wavevector are excited. However, it is important to note that the exchange-dominated magnons can also be excited under some circumstances. Hence, it is important to consider the effects discussed above in the actual physical processes leading to the observed phenomena.

As a side remark, we would like to point out that the points for which we constructed the wave packets in Fig. 6 contribute largely to the magnon DOS. Looking at the data presented in Fig. 3e reveals that at an energy of 66 meV the magnons exhibit a very large DOS. The magnon DOS at this point is almost entirely determined by the magnons localized in the interface layer. At an energy of 180 meV also the magnon DOS is large. In this part, the surface magnons contribute largely to these states. The large density of magnon states at these points would lead to a large contribution of these magnons to the overall properties of the system. Hence, these magnons would govern the static as well as dynamic properties of the system.

The behavior of the magnons describing the $n = 1$ magnon band is very similar to the Shockley surface states at some metallic surfaces, for example, Cu(111), Ag(111), and Au(111). In addition to the exciting physics of these states, an interesting feature of surface electronic states, in particular the Shockley states, is that they have been used to build up exotic quantum states^{55,56} or periodic structures⁵⁷ at surfaces. In a similar manner, magnon surface states might be used for such purposes. The core idea is very similar to that of the surface electronic states. One should bear in mind that magnons represent a fine variation of magnetization in real time and space, which might be utilized for local modulation of the spin state. Exploiting the high-wavevector

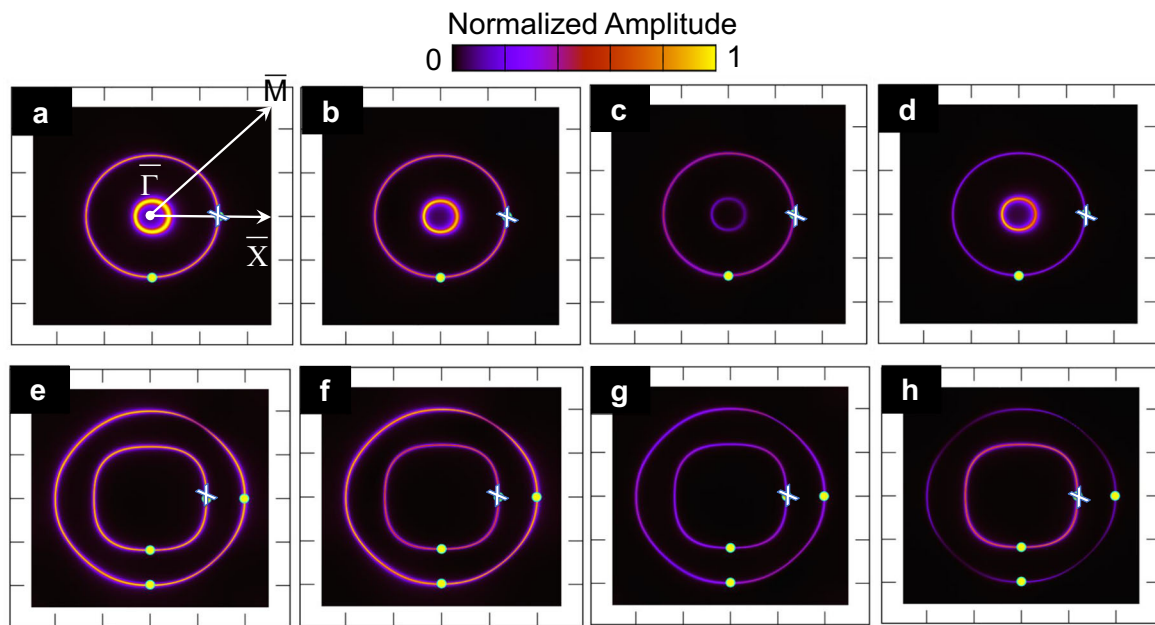


Fig. 7 Two-dimensional momentum space distribution of magnons in the Co/Fe/Co system. The energy cuts are chosen so that the wavevector of 0.7 \AA^{-1} along the high symmetry $\bar{\Gamma}$ - \bar{X} is highlighted ($\bar{\Gamma}$ and \bar{X} represent the high symmetry points of the surface Brillouin zone). This corresponds to the outer ring in panels (a-d) and the inner ring in panels (e-h). The other rings are due to the magnons with other wavevectors, which share the same energy. Panels a-d are the results for the magnon energy of 76 meV (magnons with $n = 0$) and e-h are the results for the magnon energy of 123 meV (magnons with $n = 1$). The total Bloch spectral function is shown in panels (a, e). The Bloch spectral function projected into the interface (b, f), middle (c, g), and surface layer (d, h) is also shown.

magnons shall lead to the realization of lateral variations on very short length scales (on the order of a few nanometers).

As a side remark, the magnonic surface states can also exhibit effects similar to the Rashba effect for electronic states. Such an effect is expected for systems with a large DMI. In such a case, the DMI field acting on the magnons plays the role of the spin-orbit field on the electrons. Consequently, the magnonic band associated with such a surface splits into two bands for the two opposite magnetization directions, when the magnon wavevector is perpendicular to the magnetization. The effect has been observed for an Fe double layer on W(110)⁵⁸⁻⁶⁰ and is in analogy to the Rashba type of splitting of the electronic surface states for the two opposite spin directions of the electrons.

We now aim to construct the wave packets representing the $n = 0$ and $n = 1$ magnon bands of the Co/Fe/Co system. The bands representing these states exhibit a very similar shape (see, for example, Fig. 2b). As an example, we analyze the magnons with the wavevector of $q_{\parallel} = q_x = 0.7 \text{ \AA}^{-1}$ along the high symmetry $\bar{\Gamma}$ - \bar{X} direction. We first analyze the distribution of these two magnon modes in the momentum space. For the $n = 0$ magnon mode, the corresponding magnon energy is 76 meV, and for the $n = 1$ magnon mode, it is ~ 123 meV. The two-dimensional momentum space distribution of all layers and the corresponding layer-resolved patterns are presented in Fig. 7. The results of the $n = 0$ magnon mode are shown in the upper row and those of the $n = 1$ magnon mode are shown in the lower row. For the magnon energy of 76 meV, the pattern of all three layers is shown in Fig. 7a, and the projected BSF into the interface, middle, and surface layer is shown in Fig. 7b-d, respectively. For the magnon energy of 123 meV, the pattern of all three layers is shown in Fig. 7e, and the projected BSF into the interface, middle, and surface layer is shown in Fig. 7f-h, respectively.

We construct the wave packet in the point indicated by the cross in Fig. 7, that is, $(q_x, q_y) = (0.7, 0)$, in the units of \AA^{-1} . The

wave packets and their evolution in real time and space are shown in Fig. 8.

In contrary to the case of Co/Co/Fe, in the present case, both magnon modes travel with a rather similar group velocity (the $n = 0$ magnon band possesses a group velocity of about $v_g = 24.3 \text{ km s}^{-1}$ and the $n = 1$ magnon band exhibits a group velocity of about $v_g = 27.2 \text{ km s}^{-1}$). While the $n = 0$ magnon mode is mainly localized in the interface layer, the $n = 1$ magnon mode is almost equally localized in the surface and interface layer. Interestingly, both modes have similar spectral weight in the interior layer. Although these modes show a rather similar group velocity, their lifetime is different ($\tau_0 = 53 \text{ fs}$ and $\tau_1 = 19 \text{ fs}$). This fact leads to some differences in the propagation characteristics of these two modes in real time, as it is apparent from Fig. 8.

The similar behavior of the magnon wave packets traveling in the surface and interface can lead to interesting features. For example, a coherent wavevector-selective excitation of the magnons at the surface can lead to a mode, which is almost equally distributed in the surface and interface layer, and a mode that is localized more strongly in the interface layer. The modes show rather similar propagation characteristics while traveling in the system. The system demonstrates a case in which the magnon conductivity similarly takes place in the surface and interface layer. This behavior of the surface and interface magnons would have direct consequences on the physical properties, which are directly linked to the magnon dynamics.

The discussion provided above is general and can be extended to many different layered structures grown on different surfaces. For example, in the case of Fe/Co/Co, one would expect that the magnetic exchange parameters in the surface Fe layer are weak, similar to those in the interface Co layer (see Supplementary Note 1 and Supplementary Fig. 1). This fact leads to a large spectral weight of the $n = 0$ in the surface Fe layer. The mode is also partially localized in the interface layer. The large spectral

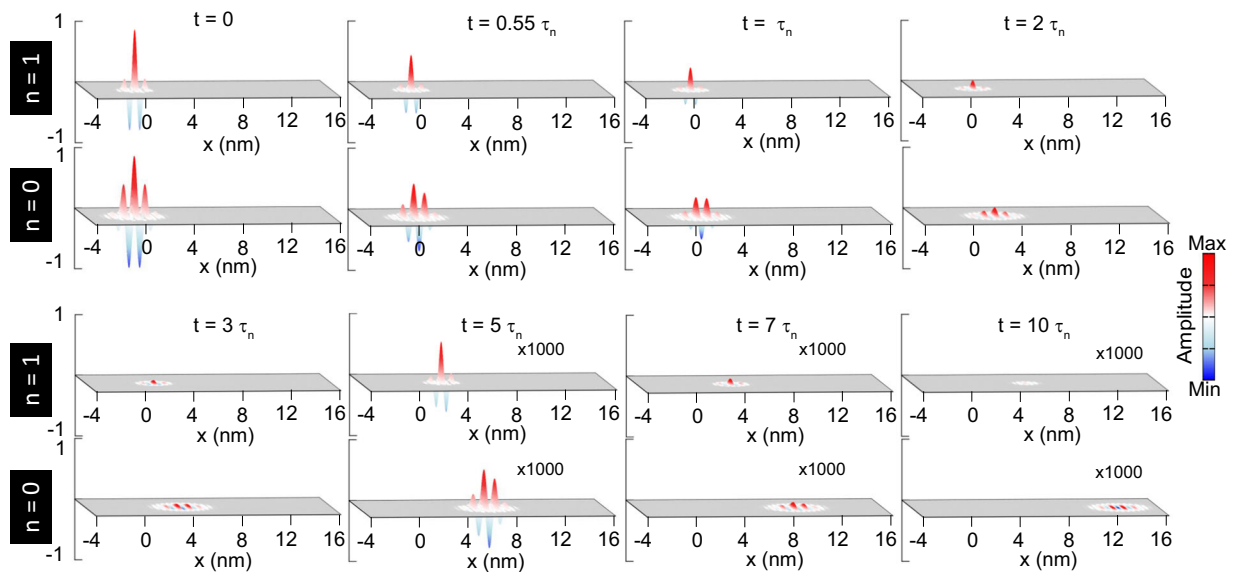


Fig. 8 Real-space evolution of surface and interface magnons in the Co/Fe/Co structure. The evolution of the magnon wave packets in the Co/Fe/Co structure at the point $(q_x, q_y) = (0.7, 0)$, indicated in Fig. 7. Here, q_x and q_y represent the x and y components of the wavevector. τ_n denotes the lifetime of the n th magnon mode and is obtained from the experimental data ($\tau_n = 2\hbar/\Gamma_n$, where Γ_n represent the intrinsic broadening of the magnon modes, $\tau_0 = 53$ fs and $\tau_1 = 19$ fs). The amplitude of the wave packets after $t = 5\tau_n$ is multiplied by 1000 for clarity.

weight of this mode in the surface Fe layer would also explain the intense excitation of this mode while performing inelastic low-energy electron scattering experiments such as SPEELS (see, for example, the spectra shown in Fig. 1c). The low spectral weight of the $n = 1$ magnon band in the surface layer, its low-energy and higher damping makes it hard to be resolved in the spectra. Similar to the discussion provided above regarding the real-space localization of magnonic bands and their consequences on the real-space dynamics of the magnon wave packets, one may also construct and discuss the wave packets in the present case.

The discussed physics can also be generalized to the newly discussed layered materials called two-dimensional magnets^{61,62} (for a review see, for example, ref. ⁶³). A similar strategy may be taken to design two-dimensional layered magnets, which exhibit desired magnonic states and magnon dynamics. We note that in the case of 2D magnets, the situation can be rather complex. Currently, two-dimensional magnets are prepared using the micromechanical exfoliation technique and multilayers may be fabricated by layer stacking. Owing to the lattice mismatches, the resulting structures will be different from the ideal model systems investigated here. Hence, novel fabrication methods need to be developed for preparing multilayers of these materials.

In summary, aiming on the understanding of the bosonic surface and interface states, we investigated the origin of the formation of magnonic band structure, surface, and interface states in layered ferromagnets. Putting magnons (bosons) within a similar formalism as electrons (fermions), we discuss the concept of the magnonic band structure in layered ferromagnets and discussed the physics of the band formation in such structures, with respect to the momentum- and real-space localization of the bands. The circumstances under which the surface and interface states may be formed were outlined. It was found that the momentum and real-space localization of magnon bands depend on the pattern of the magnetic exchange interaction. By providing various experimental examples of engineered synthetic layered structures, we verified our discussions. We demonstrated how one can design systems with strongly localized surface and interface states and how such states may exhibit mixed properties. Moreover, we showed that in the case that the pattern of the magnetic

exchange parameters in the surface or interface layers is complex and includes antiferromagnetic interactions, the surface or interface states exhibit peculiar features, for example, “standing bosonic Bloch states.” We anticipate that these states would change the static as well as dynamic properties of the material. In the context of magnon transport, one can realize different class of materials with respect to their magnon conductivity, for example, magnon conductor and insulator. Similarly, one may also extend the discussion to more exotic magnonic materials, for example, magnon Dirac, Weyl materials, and so on.

As the final remark, in our experiments, we deal with the finite number of atomic layers, which are infinite in the x - y plane. Due to the infinitely large lateral extension of our samples, it is not necessary to consider modes associated with the vertical faces. However, the physics discussed here can be extended to laterally confined systems. The subject has become recently of interest in the context of magnonic crystals^{64,65}.

Methods

Experiments

Sample preparation. All experiments were performed under ultrahigh vacuum conditions. Before film deposition, the surface of the Ir(001) substrate was cleaned using our standard cleaning procedure developed for refractory metals and described in details elsewhere⁶⁶. The alternating layers were grown by molecular beam epitaxy at 300 K. Low-energy electron diffraction recorded on the grown layered ferromagnets showed a sharp (1×1) pattern, indicating a well-ordered face-centered tetragonal structure of the multilayer structures⁶⁷. Three different synthetic layered structures were prepared and examined, namely Co/Co/Fe/Ir(001), Co/Fe/Co/Ir(001), and Fe/Co/Co/Ir(001). The results were compared to those of Co/Co/Co/Ir(001). In this representation, the thickness of each layer is one atomic layer (ML).

The magnetic state of the samples was checked by means of the magneto-optical Kerr effect in the longitudinal geometry. A rectangular ferromagnetic hysteresis loop was observed for all systems. The magnetization of the samples was found to lie in the plane for all layered structures.

Probing the magnon band structure. The magnons were probed by means of SPEELS^{41,68}. The spectra were recorded along the main symmetry directions of the SBZ at the magnetic remanent state. The incident electron energy was between 6 and 9 eV. The incident energy was chosen such that the largest magnon signal was observed in the spectra. The energy resolution was between 11 and 18 meV. Electrons with their spin parallel to the sample magnetization are referred to as minority electrons and those with spin polarization antiparallel to the sample

magnetization are referred to as majority electrons. Due to the conservation rule of the total angular momentum, magnons are excited by the incidence of minority electrons. This leads to a peak only in the minority spin spectra (I_{\downarrow}) and, consequently, a peak in the difference spectra, defined as $I_{\downarrow} - I_{\uparrow}$ ⁶⁹. The desired wavevector is achieved by changing the scattering geometry, that is, by varying the angle between the incident and scattered beam with respect to the surface normal.

The magnon band structure was constructed by probing the excitation energy of different magnon modes as a function of wavevector along the main symmetry axes of the SBZ. The measured difference spectra were fitted with a convolution of a Lorentzian and a Gaussian for each magnon mode, where the Lorentzian represents the intrinsic magnon signal and the Gaussian represents the experimental broadening. The peak position provides the magnons' energy and the intrinsic Lorentzian linewidth provides information on the magnons' lifetime. The error bars in the magnons' energy are given by the statistical and systematic uncertainties. The statistical uncertainties are given by the goodness of the fits and the deviations between the results of measurements repeated at a certain wavevector. The systematic error bars are estimated by the uncertainty in the momentum, that is, the momentum resolution. In our experiment, the momentum resolution is $\Delta q = 0.03 \text{ \AA}^{-1}$. This leads to a systematic error of a certain magnon mode with the energy of $\hbar\omega_0$ and the wavevector q_0 being $\frac{\partial \hbar\omega}{\partial q} \Big|_{q=q_0} \Delta q$, where

$\frac{\partial \hbar\omega}{\partial q} \Big|_{q=q_0}$ represents the slope of the given magnon band at q_0 and $\hbar\omega_0$.

Theory. In order to calculate the magnonic band structure in layered structures, we use a combination of modeling and ab initio calculations. The density functional theory based ab initio calculations were utilized for single-element multilayers, that is, Co and Fe films. An atomistic spin model based on the Heisenberg Hamiltonian was used to describe the magnon bands in the synthetic multilayers made of different elements. In the following, we describe both approaches.

Ab initio density functional theory calculations of magnon properties. Ab initio calculations were performed for single-element ferromagnetic atomic layers with different geometrical structures. We start with self-consistent calculations of electronic structures within the framework of a generalized gradient approximation of the density functional theory. We adopted the Korrinǵa–Kohn–Rostoker Green function method, which is specially designed for layered semi-infinite systems. The Heisenberg exchange constants were obtained by using the magnetic force theorem; likewise, implemented within the Green function method⁷⁰. In order to properly account for the interface reconstruction, a numerical scheme based on the coherent potential approximation was used^{71–73}. These calculations are carried out for the case of Co and Fe films with different geometrical structures. We used the lattice parameters reported in earlier experiments⁶⁷. The experimental geometrical parameters are used as the input in our ab initio calculations.

It is well known that first-principles calculations describe qualitatively the magnonic band structure rather well. However, they overestimate the magnon energies in Co films^{39,74–83}. This is likely due to the fact that structural and electronic structures of Co films cannot be described adequately within the single-particle density functional theory. A solution to this problem has already been discussed in ref. ³². The calculated electronic structures are modified such that to reproduce the available photoemission data, experimentally measured on the systems. The magnonic band structure calculated in this way agrees both qualitatively and quantitatively with the experimental results^{32,84}.

Calculations of magnonic band structure based on a Heisenberg model. For the case of synthetic multilayers composed of different elements, the ab initio calculations could provide a very good qualitative agreement with experimental data. However, a quantitative agreement was only achieved when all the details of electronic structures were described by the self-consistent calculations. It was realized that when the system becomes complex, it is not easy to describe the electronic structures with all the details. In order to avoid further complications, we used a Heisenberg model to calculate the magnonic band structure. In this model, we used the intralayer exchange parameters in each atomic layer, which were either calculated by means of our ab initio theory for single-element systems, as described above, or were taken from the earlier experiments, performed on single-element films grown on the same substrate, with minimum modifications. Mainly, the interlayer exchange coupling constants, describing the interaction between Fe and Co atomic layers, were varied in order to achieve a quantitative agreement with the experimental data. Within this model, up to 20 neighbors were considered, depending on the strength of the interactions.

Data availability

The datasets generated and/or analyzed during the current study are available from the corresponding author on reasonable request.

Code availability

The codes associated with this manuscript are available from the corresponding author on reasonable request.

Received: 22 July 2020; Accepted: 22 November 2020;

Published online: 04 February 2021

References

- Greig, D. *Electrons in Metals and Semiconductors*, European Physics Series (McGraw-Hill, 1969).
- Ashcroft, N. W. & Mermin, N. D. *Solid State Physics*, HRW International Editions (Holt, Rinehart and Winston, 1976).
- Kittel, C. *Introduction to Solid State Physics* (Wiley, 2004)
- Bloch, F. Über die quantenmechanik der elektronen in kristallgittern. *Z. Physik* **52**, 555–600 (1929).
- Shockley, W. On the surface states associated with a periodic potential. *Phys. Rev.* **56**, 317–323 (1939).
- Tamm, I. E. On the possible bound states of electrons on a crystal surface. *Phys. Z. Sowjetunion* **1**, 733–735 (1932).
- Davison, S. G. & Steslicka, M. *Basic Theory of Surface States*, Monographs on the Physics (Clarendon Press, 1996).
- Brillson, L. J. *Surfaces and Interfaces of Electronic Materials*, Ch. 4, 37–65 (Wiley, 2012).
- Zak, J. Symmetry criterion for surface states in solids. *Phys. Rev. B* **32**, 2218–2226 (1985).
- Zak, J. Berry's phase for energy bands in solids. *Phys. Rev. Lett.* **62**, 2747–2750 (1989).
- Hasan, M. Z. & Kane, C. L. Colloquium: topological insulators. *Rev. Mod. Phys.* **82**, 3045–3067 (2010).
- Shen, S. Q. *Topological Insulators: Dirac Equation in Condensed Matter*, Springer Series in Solid-State Sciences (Springer Singapore, 2017)
- Weyl, H. Elektron und gravitation. I. *Z. Physik* **56**, 330–352 (1929).
- Yan, B. & Felsler, C. Topological materials: Weyl semimetals. *Annu. Rev. Condens. Matter Phys.* **8**, 337–354 (2017).
- Armitage, N. P., Mele, E. J. & Vishwanath, A. Weyl and dirac semimetals in three-dimensional solids. *Rev. Mod. Phys.* **90**, 015001 (2018).
- Ibach, H. & Mills, D. *Electron Energy Loss Spectroscopy and Surface Vibrations* 105–120 (Academic, 1982).
- Jacqmin, T. et al. Direct observation of dirac cones and a flatband in a honeycomb lattice for polaritons. *Phys. Rev. Lett.* **112**, 116402 (2014).
- Banerjee, S., Fransson, J., Black-Schaffer, A. M., Ågren, H. & Balatsky, A. V. Granular superconductor in a honeycomb lattice as a realization of bosonic dirac material. *Phys. Rev. B* **93**, 134502 (2016).
- Pershoguba, S. S. Dirac magnons in honeycomb ferromagnets. *Phys. Rev. X* **8**, 011010 (2018).
- Mook, A., Henk, J. & Mertig, I. Edge states in topological magnon insulators. *Phys. Rev. B* **90**, 024412 (2014).
- Mook, A., Henk, J. & Mertig, I. Topologically nontrivial magnons at an interface of two kagome ferromagnets. *Phys. Rev. B* **91**, 224411 (2015).
- Owerre, S. A. A first theoretical realization of honeycomb topological magnon insulator. *J. Phys.* **28**, 386001 (2016).
- Owerre, S. A. Topological magnon bands and unconventional thermal hall effect on the frustrated honeycomb and bilayer triangular lattice. *J. Phys.* **29**, 385801 (2017).
- Kondo, H., Akagi, Y. & Katsura, H. Three-dimensional topological magnon systems. *Phys. Rev. B* **100**, 144401 (2019).
- Zhang, H. et al. Topological magnon bands in a room-temperature kagome magnet. *Phys. Rev. B* **101**, 100405 (2020).
- Wolfram, T. & De Wames, R. E. Surface dynamics of magnetic materials. *Progr. Surf. Sci.* **2**, 233–330 (1972).
- Puszkariski, H. Theory of surface states in spin wave resonance. *Progr. Surf. Sci.* **9**, 191–247 (1979).
- Levy, J. C. S. Surface and interface magnons: magnetic structures near the surface. *Surf. Sci. Rep.* **1**, 39–119 (1981).
- Cottam, M. G. & Tilley, D. R. *Introduction to Surface and Superlattice Excitations* (CRC Press, 2019).
- Camley, R. E. & Stamps, R. L. Magnetic multilayers: spin configurations, excitations and giant magnetoresistance. *J. Phys.* **5**, 3727–3786 (1993).
- Gurevich, A. G. *Magnetization Oscillations and Waves* (CRC Press, 1996).
- Chen, Y.-J. et al. Group velocity engineering of confined ultrafast magnons. *Phys. Rev. Lett.* **119**, 267201 (2017).
- Zakeri, K. Magnonic crystals: towards terahertz frequencies. *J. Phys.* **32**, 363001 (2020).
- Zakeri, K. et al. Direct probing of the exchange interaction at buried interfaces. *Nat. Nanotechnol.* **8**, 853–858 (2013).
- Meng, Y. et al. Direct evidence of antiferromagnetic exchange interaction in Fe (001) films: strong magnon softening at the high-symmetry \bar{M} point. *Phys. Rev. B* **90**, 174437 (2014).

36. Zakeri, K. Probing of the interfacial Heisenberg and Dzyaloshinskii-Moriya exchange interaction by magnon spectroscopy. *J. Phys.* **29**, 013001 (2016).
37. Prokop, J. et al. Magnons in a ferromagnetic monolayer. *Phys. Rev. Lett.* **102**, 177206 (2009).
38. Bergman, A. et al. Magnon softening in a ferromagnetic monolayer: a first-principles spin dynamics study. *Phys. Rev. B* **81**, 144416 (2010).
39. Qin, H. J. et al. Magnons in ultrathin ferromagnetic films with a large perpendicular magnetic anisotropy. *Phys. Rev. B* **88**, 020404 (2013).
40. Zhang, Y., Chuang, T.-H., Zakeri, K. & Kirschner, J. Relaxation time of terahertz magnons excited at ferromagnetic surfaces. *Phys. Rev. Lett.* **109**, 087203 (2012).
41. Zakeri, K. & Kirschner, J. in *Topics in Applied Physics* 83–99 (eds Demokritov, S. O. & Slavin, A. N.) (Springer, 2012).
42. Qin, H. J. et al. Long-living terahertz magnons in ultrathin metallic ferromagnets. *Nat. Commun.* **6**, 6126 (2015).
43. Slonczewski, J. C. Current-driven excitation of magnetic multilayers. *J. Magn. Magn. Mater.* **159**, L1–L7 (1996).
44. Myers, E. B., Ralph, D. C., Katine, J. A., Louie, R. N. & Buhrman, R. A. Current-induced switching of domains in magnetic multilayer devices. *Science* **285**, 867–870 (1999).
45. Tsoi, M. et al. Generation and detection of phase-coherent current-driven magnons in magnetic multilayers. *Nature* **406**, 46–48 (2000).
46. Katine, J. A., Albert, F. J., Buhrman, R. A., Myers, E. B. & Ralph, D. C. Current-driven magnetization reversal and spin-wave excitations in Co/Cu/Co pillars. *Phys. Rev. Lett.* **84**, 3149–3152 (2000).
47. Grollier, J. et al. Spin-polarized current induced switching in Co/Cu/Co pillars. *Appl. Phys. Lett.* **78**, 3663–3665 (2001).
48. Urazhdin, S., Birge, N. O., Pratt, W. P. & Bass, J. Current-driven magnetic excitations in permalloy-based multilayer nanopillars. *Phys. Rev. Lett.* **91**, 146803 (2003).
49. Kent, A. D., Özyilmaz, B. & delBarco, E. Spin-transfer-induced precessional magnetization reversal. *Appl. Phys. Lett.* **84**, 3897–3899 (2004).
50. Huai, Y., Albert, F., Nguyen, P., Pakala, M. & Valet, T. Observation of spin-transfer switching in deep submicron-sized and low-resistance magnetic tunnel junctions. *Appl. Phys. Lett.* **84**, 3118–3120 (2004).
51. Yagami, K., Tulapurkar, A. A., Fukushima, A. & Suzuki, Y. Low-current spin-transfer switching and its thermal durability in a low-saturation-magnetization nanomagnet. *Appl. Phys. Lett.* **85**, 5634–5636 (2004).
52. Seki, T., Mitani, S., Yakushiji, K. & Takanashi, K. Spin-polarized current-induced magnetization reversal in perpendicularly magnetized L1₀-FePt layers. *Appl. Phys. Lett.* **88**, 172504 (2006).
53. Liu, L. et al. Spin-torque switching with the giant spin hall effect of tantalum. *Science* **336**, 555–558 (2012).
54. Yu, G. et al. Switching of perpendicular magnetization by spin-orbit torques in the absence of external magnetic fields. *Nat. Nanotechnol.* **9**, 548–554 (2014).
55. Crommie, M. F., Lutz, C. P. & Eigler, D. M. Confinement of electrons to quantum corrals on a metal surface. *Science* **262**, 218–220 (1993).
56. Ball, P. Quantum objects on show. *Nature* **462**, 416–416 (2009).
57. Ding, H. F. et al. Self-organized long-period adatom strings on stepped metal surfaces: scanning tunneling microscopy, ab initio calculations, and kinetic monte carlo simulations. *Phys. Rev. B* **76**, 033409 (2007).
58. Costa, A. T., Muniz, R. B., Lounis, S., Klautau, A. B. & Mills, D. L. Spin-orbit coupling and spin waves in ultrathin ferromagnets: the spin-wave Rashba effect. *Phys. Rev. B* **82**, 014428 (2010).
59. Zakeri, K. et al. Asymmetric spin-wave dispersion on Fe(110): direct evidence of the Dzyaloshinskii-Moriya interaction. *Phys. Rev. Lett.* **104**, 137203 (2010).
60. Zakeri, K., Zhang, Y., Chuang, T.-H. & Kirschner, J. Magnon lifetimes on the Fe(110) surface: the role of spin-orbit coupling. *Phys. Rev. Lett.* **108**, 197205 (2012).
61. Gong, C. et al. Discovery of intrinsic ferromagnetism in two-dimensional van der waals crystals. *Nature* **546**, 265–269 (2017).
62. Huang, B. et al. Layer-dependent ferromagnetism in a van der waals crystal down to the monolayer limit. *Nature* **546**, 270–273 (2017).
63. Cortie, D. L. et al. Two-dimensional magnets: Forgotten history and recent progress towards spintronic applications. *Adv. Funct. Mater.* **30**, 1901414 (2019).
64. Lisenkov, I. et al. Spin-wave edge modes in finite arrays of dipolarly coupled magnetic nanopillars. *Phys. Rev. B* **90**, 104417 (2014).
65. Rychlý, J. & Klos, J. W. Spin wave surface states in 1d planar magnonic crystals. *J. Phys. D* **50**, 164004 (2017).
66. Zakeri, K., Peixoto, T. R. F., Zhang, Y., Prokop, J. & Kirschner, J. On the preparation of clean tunneling single crystals. *Surf. Sci.* **604**, L1–L3 (2010).
67. Heinz, K. & Hammer, L. Nanostructure formation on ir(100). *Progr. Surf. Sci.* **84**, 2–17 (2009).
68. Zakeri, K. Elementary spin excitations in ultrathin itinerant magnets. *Phys. Rep.* **545**, 47–93 (2014).
69. Vollmer, R., Eitzkorn, M., Anil Kumar, P. S., Ibach, H. & Kirschner, J. Spin-polarized electron energy loss spectroscopy of high energy, large wave vector spin waves in ultrathin fcc Co films on Cu(001). *Phys. Rev. Lett.* **91**, 147201 (2003).
70. Liechtenstein, A. I., Katsnelson, M. I., Antropov, V. P. & Gubanov, V. A. Local spin density functional approach to the theory of exchange interactions in ferromagnetic metals and alloys. *J. Magn. Magn. Mater.* **67**, 65–74 (1987).
71. Soven, P. Coherent-potential model of substitutional disordered alloys. *Phys. Rev.* **156**, 809–813 (1967).
72. Gyorffy, B. L. Coherent-potential approximation for a nonoverlapping-muffin-tin-potential model of random substitutional alloys. *Phys. Rev. B* **5**, 2382–2384 (1972).
73. Buczek, P. et al. Spin waves in disordered materials. *J. Phys.* **30**, 423001 (2018).
74. Costa, A. T., Muniz, R. B. & Mills, D. L. Theory of spin waves in ultrathin ferromagnetic films: The case of Co on Cu(100). *Phys. Rev. B* **69**, 064413 (2004).
75. Taroni, A., Bergman, A., Bergqvist, L., Hellsvik, J. & Eriksson, O. Suppression of standing spin waves in low-dimensional ferromagnets. *Phys. Rev. Lett.* **107**, 037202 (2011).
76. Chuang, T.-H. et al. Impact of atomic structure on the magnon dispersion relation: a comparison between Fe(111)/Au/W(110). *Phys. Rev. Lett.* **109**, 207201 (2012).
77. Bergqvist, L., Taroni, A., Bergman, A., Eitz, C. & Eriksson, O. Atomistic spin dynamics of low-dimensional magnets. *Phys. Rev. B* **87**, 144401 (2013).
78. Balashov, T., Buczek, P., Sandratskii, L., Ernst, A. & Wulfschel, W. Magnon dispersion in thin magnetic films. *J. Phys.* **26**, 394007 (2014).
79. Eriksson, O., Bergman, A., Bergqvist, L. & Hellsvik, J. *Atomistic Spin Dynamics: Foundations and Applications* (Oxford Univ. Press, 2016).
80. Rajeswari, J. et al. Surface spin waves of fcc cobalt films on Cu(100): high-resolution spectra and comparison to theory. *Phys. Rev. B* **86**, 165436 (2012).
81. Rajeswari, J., Ibach, H. & Schneider, C. M. Standing spin waves in ultrathin magnetic films: a method to test for layer-dependent exchange coupling. *Phys. Rev. Lett.* **112**, 127202 (2014).
82. Ibach, H. High resolution electron energy loss spectroscopy of spin waves in ultra-thin film: the return of the adiabatic approximation? *Surf. Sci.* **630**, 301–310 (2014).
83. Michel, E., Ibach, H. & Schneider, C. M. Spin waves in ultrathin hexagonal cobalt films on W(110), Cu(111), and Au(111) surfaces. *Phys. Rev. B* **92**, 024407 (2015).
84. Qin, H. J., Tsurkan, S., Ernst, A. & Zakeri, K. Experimental realization of atomic-scale magnonic crystals. *Phys. Rev. Lett.* **123**, 257202 (2019).

Acknowledgements

K.Z. acknowledges funding from the Deutsche Forschungsgemeinschaft (DFG) through the Heisenberg Program ZA 902/3-1 and ZA 902/6-1 and the DFG Grant No. ZA 902/4-1. H.Q. acknowledges funding from the Academy of Finland (Grant No. 317918). The work of A.E. was supported by the DFG via the Collaborative Research Center 762 (Project No. A4). K.Z. thanks the Physikalisches Institut for hosting the group and providing the necessary infrastructure.

Author contributions

K.Z. initiated the idea of the study, supervised the whole project, conceived and planned the experiments, participated in the analysis of the experimental data, performed the calculations based on the Heisenberg model, and wrote the paper. H.Q. carried out the experiments and analyzed the experimental data. A.E. performed the first-principles calculations.

Competing interests

The authors declare no competing interests.

Additional information

Supplementary information The online version contains supplementary material available at <https://doi.org/10.1038/s42005-021-00521-7>.

Correspondence and requests for materials should be addressed to K.Z.

Reprints and permission information is available at <http://www.nature.com/reprints>

Publisher's note Springer Nature remains neutral with regard to jurisdictional claims in published maps and institutional affiliations.



Open Access This article is licensed under a Creative Commons Attribution 4.0 International License, which permits use, sharing, adaptation, distribution and reproduction in any medium or format, as long as you give appropriate credit to the original author(s) and the source, provide a link to the Creative Commons license, and indicate if changes were made. The images or other third party material in this article are included in the article's Creative Commons license, unless indicated otherwise in a credit line to the material. If material is not included in the article's Creative Commons license and your intended use is not permitted by statutory regulation or exceeds the permitted use, you will need to obtain permission directly from the copyright holder. To view a copy of this license, visit <http://creativecommons.org/licenses/by/4.0/>.

© The Author(s) 2021